

Millisecond-long electron spin lifetime in CsPbI₃ perovskite nanocrystals revealed by optically detected magnetic resonance

Vasilii V. Belykh,^{1,*} Mikhail M. Glazov,² Sergey R. Meliakov,^{1,3} Dmitri R. Yakovlev,^{1,2,3} Evgeniya V. Kulebyakina,³ Mikhail L. Skorikov,³ Mikhail V. Kochiev,³ Maria S. Kuznetsova,⁴ Elena V. Kolobkova,^{5,6} and Manfred Bayer^{1,7}

¹*Experimentelle Physik 2, Technische Universität Dortmund, 44227 Dortmund, Germany*

²*Ioffe Institute, Russian Academy of Sciences, 194021 St. Petersburg, Russia*

³*P.N. Lebedev Physical Institute of the Russian Academy of Sciences, 119991 Moscow, Russia*

⁴*Spin Optics Laboratory, St. Petersburg State University, 198504 St. Petersburg, Russia*

⁵*ITMO University, 199034 St. Petersburg, Russia*

⁶*St. Petersburg State Institute of Technology, 190013 St. Petersburg, Russia*

⁷*Research Center FEMS, Technische Universität Dortmund, 44227 Dortmund, Germany*

(Dated: March 4, 2026)

Perovskite nanocrystals are a convenient model system for optical spin orientation and manipulation. However, its real potential might be underestimated due to the incomplete knowledge on spin relaxation times, which are obscured by the limited sensitivity of measurement techniques as well as by the insufficient understanding of the spin relaxation mechanisms in perovskites. In this work, we study the spin relaxation of charge carriers in perovskite nanocrystals both experimentally and theoretically. We address the electron and hole spins in CsPbI₃ nanocrystals embedded in a glass matrix by the resonant spin inertia technique based on optically detected magnetic resonance. It allows us to determine the longitudinal spin relaxation time T_1 separately for electrons and holes, the g factors, and the effective Overhauser field of the nuclear spin bath. At a temperature of 1.6 K, the T_1 time for electrons can be as long as 0.9 ms. We reveal the effect of the time-varying nuclear field fluctuations, which enhances the electron spin relaxation at low magnetic fields, and measure a rather long nuclear spin correlation time of about 60 μ s. We develop a model of the spin relaxation in nanocrystals based on a two-LO-phonon Raman process, which explains the observed temperature dependence of the time T_1 .

I. INTRODUCTION

Lead halide perovskite semiconductors have recently attracted great attention as a promising material for solar cells [1–3]. This has stimulated intense investigations of perovskites beyond photovoltaics that revealed potential for their application as X-ray detectors [4, 5], light-emitting diodes [6–8], quantum emitters [9], etc. Lead halide perovskites are optically active (direct band gap) semiconductors with transition energies lying in the visible or near infrared range. They can be synthesized in the form of bulk single crystals with a well defined optical transition energy or nanocrystals (NCs), where the transition energy (and emission wavelength) can be tailored by varying the NC size and composition [10]. Perovskite NCs embedded in glass matrix [11] as studied in this work demonstrate the robustness with respect to the environment.

Perovskites demonstrate interesting spin properties, which can be studied by the optical techniques developed for traditional semiconductors [12–22]. Unlike in prototypical GaAs, both the electrons and the holes at the bottom of the conduction band and the top of the valence band, respectively, carry spin 1/2 [23]; perovskites feature a stronger hyperfine interaction with the nuclear spins for the holes compared to that for the electrons

[24, 25]. They show nanosecond spin coherence times at room temperature [26, 27], also because of the lack of the Dyakonov-Perel relaxation mechanism, as confirmed by strong optical orientation under nonresonant excitation [28, 29].

The possibility of practical applications of a spin system depends on the values of the spin lifetimes T_1 and T_2 . The spin coherence time T_2 , which characterizes the unperturbed spin precession about a magnetic field, determines the applicability of a spin state as a qubit. On the other hand, the relaxation time T_1 of a spin along the magnetic field sets the ultimate limit for T_2 , when it is extended by decoupling protocols. In perovskites, T_1 and T_2 are only little explored mainly due to limitations of the applied techniques. The spin coherence time T_2 is obscured by the spread of g factors and by nuclear field fluctuations in pump-probe experiments. As a result, these experiments reveal the inhomogeneous spin dephasing time T_2^* of a few ns rather than the spin coherence time T_2 [15, 16]. On the other hand, the extended pump-probe experiments show that the longitudinal spin dynamics is nonexponential and only $T_1 = 100$ ns corresponding to its fast component of about 100 ns was determined [24, 30] so far. Measurements over longer time scales are complicated by the weak signal resulting from the low repetition rates of the laser pulses. Furthermore, standard measurements of the longitudinal spin relaxation (photoluminescence dynamics with polarization control and pump-probe experiments) cannot answer whether the obtained relaxation time should be attributed to electrons

* vasilii.belykh@tu-dortmund.de

or to holes. Recently, a novel technique that exploits optically detected magnetic resonance (ODMR) with detection of the Faraday rotation combined with the spin inertia effect was developed. This technique, referred to as resonant spin inertia, makes it possible to measure the time T_1 for carriers with a distinct value of the g factor and, therefore, attribute T_1 to electrons or holes [31]. It was applied to CsPb(Cl,Br)₃ NCs at low magnetic fields, where a submillisecond-long time T_1 was measured and attributed to the spatially indirect exciton [32].

In this study, we apply this ODMR-based resonant spin inertia technique to CsPbI₃ NCs, clearly observe electron and hole resonances and measure the corresponding g factors as well as longitudinal spin relaxation times T_1 . We show that the electron T_1 increases with magnetic field due to the suppression of the effect of fluctuating nuclear fields on the electron spin relaxation. This dependence makes it possible to estimate the characteristic time of the nuclear field variations, which appears to be much longer than that reported for, e.g., GaAs quantum dots [33]. For relatively high magnetic fields, low laser powers, and a temperature of 1.6 K, we find the electron T_1 to be as long as 0.9 ms, which, to the best of our knowledge, is the longest value reported for perovskite NCs. The temperature dependence of T_1 shows an activation-like behavior with a characteristic energy corresponding to a low-frequency LO phonon energy in the CsPbI₃ perovskite. We develop a theory of spin relaxation in perovskite NCs based on a two-phonon Raman process, which accounts for the experimental findings.

II. EXPERIMENTAL DETAILS

The samples under study are CsPbI₃ NCs embedded in a fluorophosphate Ba(PO₃)₂-AlF₃ glass matrix. They were synthesized by rapid cooling of a glass melt enriched with the components needed for perovskite crystallization as described in Refs. [11, 20, 34, 35]. Two samples, in the following referred to as #1 and #2 (technological codes EK202 and EK8-M), with average NC sizes ranging from 7 to 14 nm are studied. The two samples show qualitatively a similar behavior of their spin properties, all results except the spectral dependences (Fig. 2) are shown for the sample #1. The sample is placed into a Helium-bath cryostat with a superconducting magnet allowing us to apply a magnetic field \mathbf{B} in the Faraday geometry (along the laser beam). All experiments are performed at a temperature of $T = 1.6$ K unless otherwise stated.

We measure the optically detected magnetic resonance stimulated by optical pumping and evaluate the longitudinal spin relaxation time T_1 with the technique described in Refs. [31, 32]. The sample is excited by the radiation of a Coherent Chameleon Discovery laser system emitting 100 fs pulses (7 nm spectral width) with a repetition rate of 80 MHz, tunable across a wide spectral range. Note that the fact that the laser is pulsed (rather

than continuous wave) is not essential for this technique as long as the separation between pulses is much smaller than the time T_1 . The laser wavelength is tuned into resonance with the fundamental optical transition of the studied NCs. The polarization of the laser beam passing the sample is set to be elliptical, so that the circularly polarized component of the beam excites carrier spin polarization in the sample. This polarization is detected by measuring Faraday rotation experienced by the linearly polarized component. The Faraday rotation was measured using a conventional scheme: the transmitted laser beam passed a half-wave plate followed by a Wollaston prism, splitting it into two beams with orthogonal linear polarizations whose intensities are then measured by a balanced photodetector. The difference signal from the photodetector is proportional to the Faraday rotation angle and, ultimately, to the spin polarization in the sample. A coil with a diameter of about 1 mm is placed near the sample surface, so that the laser beam passes through both the sample and the coil. The coil is used to apply a radiofrequency (rf) magnetic field with frequency up to 4 GHz to the sample.

Thus, the spin polarization is created and detected using the optical beam, while the rf field applied in resonance with the Larmor spin precession frequency destroys the spin polarization [31]. The rf power is modulated at the frequency f_{mod} ranging from 0.1 to 100 kHz and the corresponding modulation of the spin polarization is detected with the balanced photodetector and a lock-in amplifier. By scanning the magnetic field with the rf frequency f_{rf} fixed, it is possible to detect the magnetic resonances for electrons and holes in the studied NCs. It is also possible to evaluate the longitudinal spin relaxation time T_1 . Indeed, the signal is independent of the rf modulation frequency f_{mod} for low frequencies, where the modulation period is longer than the time T_1 . At higher frequencies, $f_{\text{mod}} \gtrsim 1/T_1$, the signal begins to decrease with f_{mod} , and so the modulation-frequency dependence of the signal makes it possible to evaluate T_1 . This is similar to the all-optical spin inertia method [36], but in contrast to it, in our case T_1 can be measured selectively for a given spin resonance (e.g., the electron or the hole) by setting the value of the rf frequency or the magnetic field; correspondingly, this method is referred to as resonant spin inertia [31].

III. ODMR SPECTRA OF PEROVSKITE NANOCRYSTALS

Figure 1(a) shows the dependence of the Faraday rotation signal on the magnetic field (ODMR spectrum) for different rf field frequencies. The spectrum at $f_{\text{rf}} = 1.0$ GHz is measured both in the positive and negative range of magnetic fields and is rather symmetric, which indicates the absence of a notable dynamic nuclear polarization. The spectra show a clear resonant behavior of the Larmor spin precession frequency and the rf field

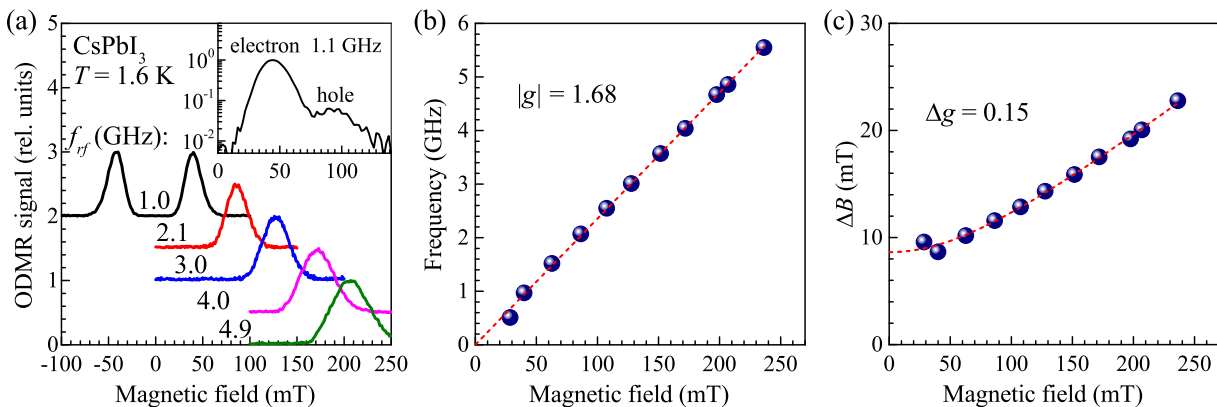


Figure 1. Optically detected magnetic resonance in CsPbI₃ NCs. (a) ODMR spectra for different rf field frequencies. The modulation frequency is 0.6 kHz, the laser photon energy is 1.824 eV, the laser power is 0.5 mW. The inset shows the ODMR spectrum for $f_{\text{rf}} = 1.1$ GHz at an increased modulation frequency of 3 kHz and a laser power of 2 mW manifesting two resonances. (b) Magnetic field dependence of the magnetic resonance frequency allowing one to determine the electron g factor of 1.68 from the linear fit shown by the red dashed line. (c) Magnetic field dependence of the width of the electron ODMR resonance (defined as the normal distribution standard deviation σ). The red dashed line shows a fit with Eq. (2). The temperature is 1.6 K.

frequency f_{rf} , described by the equation

$$2\pi\hbar f_{\text{rf}} = |g|\mu_{\text{B}}B, \quad (1)$$

where g is the g factor and μ_{B} is the Bohr magneton. As the rf field frequency is increased, the resonance peak shifts towards higher fields and broadens. Figure 1(b) shows the resonance frequency as a function of the magnetic-field position of the peak. The dependence is linear with the slope corresponding to a g factor of 1.68. The value of this g factor at the energy of 1.824 eV indicates that it belongs to electrons and its sign is positive, according to theoretical predictions [37].

The ODMR peak can be well fitted by a Gaussian distribution with the standard deviation σ giving the width of the ODMR peak ΔB . The width increases with growing magnetic field [Fig. 1(c)]. This increase is related to the spread of g factors Δg [38] and can be described by the equation

$$\Delta B = \left[\Delta_{\text{N}}^2/2 + \left(\frac{\Delta g}{g} B \right)^2 \right]^{1/2}. \quad (2)$$

This equation assumes that the finite width of the ODMR peak is contributed by the spread of Larmor frequencies resulting from the Gaussian distribution of g factors with standard deviation Δg and by the Gaussian distribution of the effective Overhauser field \mathbf{B}_{N} of the nuclear spin fluctuations $\pi^{-3/2}\Delta_{\text{N}}^{-3}\exp(-\mathbf{B}_{\text{N}}^2/\Delta_{\text{N}}^2)$ with Δ_{N} being the spread of the nuclear field fluctuations [39, 40]. The Δg contribution can be evaluated from Eq. (1). The convolution of these two Gaussian distributions results in a Gaussian distribution with the standard deviation given by Eq. (2). Fitting the dependence of ΔB on B [Fig. 1(c)] with Eq. (2), we determine $\Delta g = 0.15$ and $\Delta_{\text{N}} \approx 12$ mT. These values are in good agreement with those obtained

from pump-probe Faraday rotation measurements on a similar sample by analyzing the electron spin precession in zero field and the precession decay in high fields [41]. Note that apart from the strong electron resonance, the ODMR spectra reveal a much weaker peak at higher fields [inset in Fig. 1(a)], corresponding to $|g| \approx 0.8$, related to holes [18, 20, 35]. Interestingly, the hole peak is observed only in a finite range of rf field frequencies, which is characteristic of the carriers within an exciton [32].

Next, we present the dependence of the electron g factor and effective nuclear field on the NC size parametrized by the optical transition energy. The sample contains an inhomogeneous ensemble of NCs with different sizes and, thus, different quantum-confinement energies resulting in a spread of their emission energies. We can address NCs of different sizes within the same sample by changing the laser photon energy. Higher energy corresponds to NCs of smaller size.

We study two samples with different average sizes of NCs to address a broader range of energies. The optical transition energy dependence of the g factor is shown in Fig. 2(b), while for reference we present the photoluminescence (PL) spectra of the samples in Fig. 2(a). The electron g factor decreases with growing energy, which corresponds to the general trend of the universal g factor dependence on the bandgap [17], confirming the electron origin of the observed resonance. A similar energy dependence of the g factor measured by a pump-probe technique for CsPbI₃ perovskite NCs is discussed in detail in Refs. 18 and 20.

Figure 2(c) shows the corresponding energy dependence of the ODMR peak width ΔB (standard deviation) at a rather small field of about 45 mT. This width mostly originates from the effective nuclear field, $\Delta B \approx \Delta_{\text{N}}/\sqrt{2}$, as one can see from Fig. 1(c) and Eq. (2). It follows from

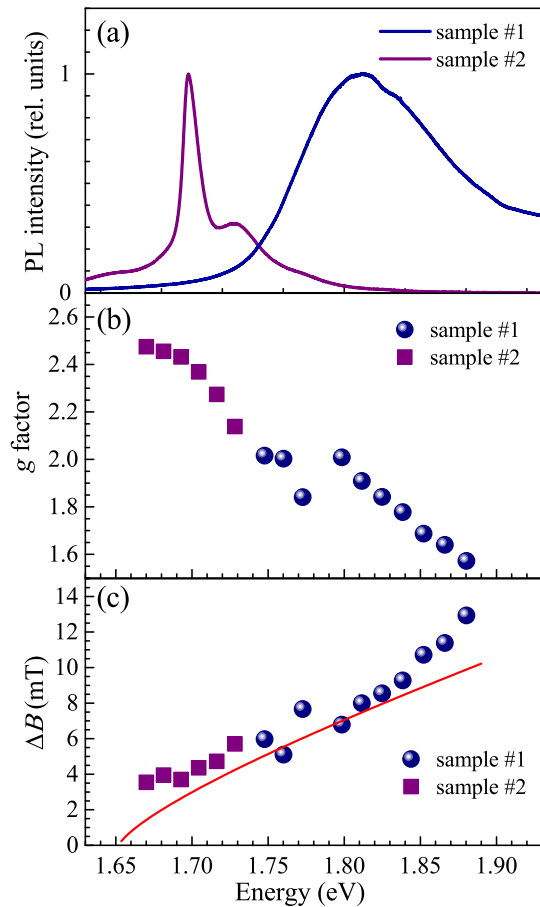


Figure 2. (a) Photoluminescence spectra of the two CsPbI₃ perovskite samples with different average NC sizes measured at $T = 6$ K. Dependence of electron g factor on optical transition energy (b) and of electron ODMR peak width (c) measured at $f_{\text{rf}} = 1.13$ GHz (magnetic field of about 45 mT). The red solid line shows the calculated nuclear field according to Ref. [41], see text. The temperature in (b) and (c) is 1.6 K.

this figure that the nuclear field increases with energy, i.e., with a decreasing NC size a . This behavior is expected, as the number of nuclear spins $N \propto a^3$ in a NC. The net spin in a NC averaged over all nuclei having random spin orientation is proportional to $N^{1/2} \propto a^{3/2}$. On the other hand, the electron wavefunction spreads over the entire NC volume, and the contribution of an individual nuclear spin to the hyperfine field sensed by the electron is proportional to a^{-3} . As a result, the total hyperfine field is proportional to $a^{3/2}a^{-3} \propto a^{-3/2}$. The proportionality coefficient depends on the hyperfine constants and the contributions of the different nuclear species. It was calculated in Ref. [41] for the same system. Using these calculations with the hyperfine constants of Pb and I of 50 and 190 μeV , respectively, we get $\Delta B \approx \Delta_N/\sqrt{2} = (a_0/a)^{3/2} \times (0.47 \text{ T})$, where $a_0 = 0.624 \text{ nm}$ is the lattice constant. To relate the transition energy to the NC size, we use Eq. (S10) from the

Supporting Information of Ref. [42]. The resulting calculated curve is shown by the red solid line in Fig. 2(c). It shows reasonable agreement with the experimental dependence. The deviation at small energies is related to the limited accuracy of the NC size estimation when the NC transition energy is close to that of bulk material.

IV. LONGITUDINAL SPIN RELAXATION TIME, T_1 : RESONANT SPIN INERTIA EXPERIMENTS

Here we turn to the measurement of the longitudinal spin relaxation time T_1 . In this experiment, we fix the magnetic field, so that the rf field is resonant with the electron (or hole) Larmor frequency and measure the ODMR signal as a function of the rf field modulation frequency f_{mod} (spin inertia curve). Figure 3(a) shows the spin inertia curves for the electron and hole resonances. The signal weakly depends on f_{mod} at low frequencies, when $f_{\text{mod}} \ll 1/T_1$. As the frequency is increased above $1/T_1$, the accumulated spin, i.e. the signal, becomes limited by the modulation period $1/f_{\text{mod}}$ rather than T_1 . This is reflected by the formula [31]

$$S = \frac{S_0}{\sqrt{1 + (2\pi T_1 f_{\text{mod}})^2}}, \quad (3)$$

where S_0 is the amplitude of the spin signal S under infinitely slow modulation. Fitting the experimental curves with this equation [red dashed lines in Fig. 3(a)] gives $T_1 = 130 \mu\text{s}$ for the electrons and $70 \mu\text{s}$ for the holes. Note that these measurements are performed for an increased excitation power of 2 mW to resolve the hole resonance. At the same time, a decrease in the laser power leads to an increase in T_1 as depicted in the inset of Fig. 3(a). The experimental dependence suggests that the rate $1/T_1$ increases linearly with power P , and extrapolation of the dependence to zero power gives $T_1 = 0.9 \text{ ms}$. The remarkably long T_1 times of electrons and holes evidence that the measured signals originate from long-living (resident) charge carriers in NCs. These carriers can arise from photogenerated electron-hole pairs, when one of the carriers is captured by the surface trap [43]. We do not exclude formation of the spatially indirect long-living excitons in the case of shallow traps.

The dependence of the electron time T_1 on the magnetic field is shown in Fig. 3(b). One can see that T_1 increases strongly with B within 60 mT and then saturates. This is the typical behaviour expected when T_1 is determined by fluctuating internal (nuclear) magnetic fields, whose impact is suppressed by the external magnetic field. This scenario was considered in Ref. [44], where the following analytical formula for $T_1(B)$ was proposed:

$$T_1 = \frac{\tau_s}{1 + (\Delta_N/B)^2 \tau_s/\tau_c}. \quad (4)$$

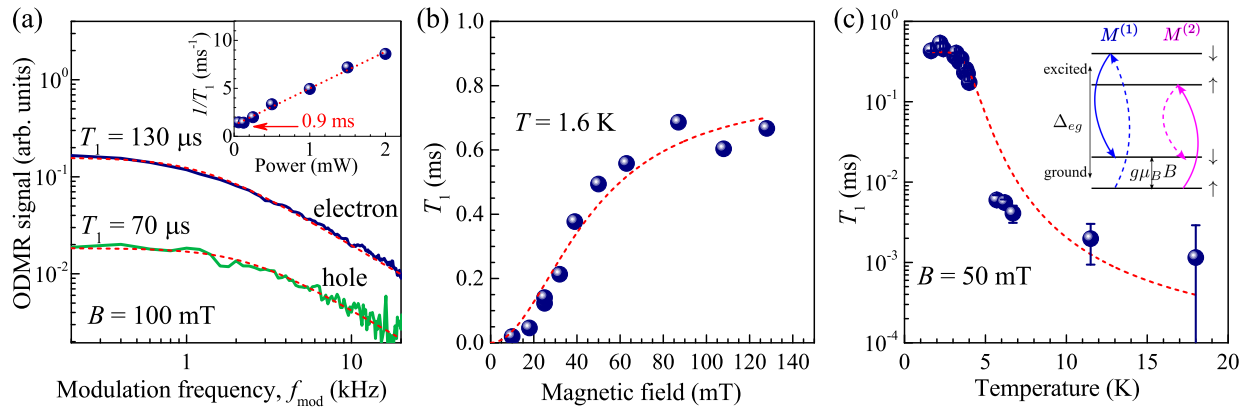


Figure 3. (a) Dependence of the ODMR signal on the modulation frequency for the electron and hole resonances for a magnetic field of 100 mT (the corresponding rf frequencies are 2.2 and 0.6 GHz) and an increased laser power of 2 mW. The curves demonstrate the spin inertia effect making it possible to determine the times T_1 for the electrons and the holes separately. The dashed lines show fits with Eq. (3). The inset shows the dependence of $1/T_1$ on the laser power for the electron with a linear fit shown by the dashed line. (b) Magnetic field dependence of the electron T_1 measured with a laser power of 0.125 mW. The dashed line shows a fit with Eq. (4). (c) Temperature dependence of the electron T_1 corresponding to a laser power of 0.125 mW. The dashed line shows a fit with an activation dependence (5). The inset shows a sketch of virtual transitions to the NC excited state, accompanied by the emission and absorption of LO phonons resulting in a spin flip. The laser photon energy is 1.824 eV. The temperature in panels (a) and (b) is 1.6 K.

Here, τ_s is the spin relaxation time limited by mechanisms other than the nuclear-field fluctuations, τ_c is the correlation time of the nuclear fluctuations characterizing evolution of the effective nuclear field within NC. This equation is valid when B exceeds the spread of nuclear fields Δ_N and the corresponding Larmor spin precession frequency exceeds $1/\tau_c$. Both conditions are satisfied in our experiments. For $B \gg \Delta_N$, Eq. (4) yields $T_1 \approx \tau_s \approx 0.8 \text{ ms}$. We can estimate $\Delta_N \approx 12 \text{ mT}$ from the width of the ODMR resonance for $B \rightarrow 0$ [Fig. 1(c) and Eq. (2)]. Fitting the dependence $T_1(B)$ with Eq. (4) [red dashed lines in Fig. 3(b)], we then obtain $\tau_c \approx 60 \mu\text{s}$. This time, characterizing the random variation of the effective nuclear field in NCs, is much longer than that reported for (In,Ga)As QDs ($\sim 1 \mu\text{s}$) [33]. We note that in CsPbI₃ NCs the hyperfine interaction for electrons is dominated by the iodine nuclei [41], which have spin 5/2, enabling their quadrupole interaction. The latter seems to be weaker than, e.g., in GaAs-based systems, as suggested by the long τ_c .

The dependence of the electron time T_1 on temperature T is shown in Fig. 3(c). This dependence is weak below 3 K, and then T_1 starts to decrease rapidly. This decrease can be described by an activation dependence, which might take place if relaxation is caused by activation to some energy level at an energy E_a above the considered state:

$$\frac{1}{T_1} = \frac{1}{T_{1,0}} + \gamma_a \exp\left(-\frac{E_a}{k_B T}\right). \quad (5)$$

Here $T_{1,0}$ is the relaxation time in the low-temperature limit and γ_a is the activation rate, k_B is the Boltzmann constant. The red dashed line in Fig. 3(c)] shows a fit

of the experimental data by this equation with parameters $E_a = 3.2 \text{ meV}$ and $\gamma_a = 20 \mu\text{s}^{-1}$. We note that this value of E_a is close to an optical-phonon energy of 3.2 meV [42, 45], which suggests that the spin relaxation process involves optical phonons. This will be confirmed by the theoretical considerations below. We note that strictly speaking we measure spin lifetime, which can be contributed by the carrier lifetime and by the time T_1 . However strong dependence of measured time on magnetic field and temperature indicates that in our case spin lifetime is dominated by T_1 . Nevertheless, we do not exclude that at lowest temperatures and high magnetic fields spin lifetime may have notable contribution from carrier lifetime.

V. THEORY OF TWO-OPTICAL PHONON INDUCED ELECTRON SPIN FLIP IN PEROVSKITE NANOCRYSTALS

Let us discuss the temperature dependence of the longitudinal spin relaxation time T_1 in more detail. We note that real activation to an excited state in NCs under study is hardly possible at low temperatures, since the corresponding energy separation is in the tens of millielectronvolts range. Thus, one has to consider virtual transitions in second-order perturbation theory involving phonons, which provide an effective Rashba-like spin-orbit coupling. For a model description, we consider a NC in the form of a cuboid with principal axes x , y , z that also correspond to the crystallographic axes. Here we disregard the reduced symmetry of the perovskite host and consider it to be in the cubic O_h phase. Let the

magnetic field $\mathbf{B} \parallel z$ be directed along one of its principal axes. We assume the interaction of charge carriers (electrons for definiteness) with bulk optical phonons via the Fröhlich (polarization) mechanism.

To that end, we recall that a longitudinal optical (LO) phonon with wavevector \mathbf{q} produces an electric potential

$$\varphi_{\mathbf{q}} = \alpha_F \frac{i}{q} \left(\hat{b}_{\mathbf{q}} e^{i\mathbf{q}\mathbf{r} - i\Omega_{\mathbf{q}}t} - \hat{b}_{\mathbf{q}}^\dagger e^{-i\mathbf{q}\mathbf{r} + i\Omega_{\mathbf{q}}t} \right), \quad (6)$$

where $\hat{b}_{\mathbf{q}}$ and $\hat{b}_{\mathbf{q}}^\dagger$ are the phonon annihilation and creation operators, respectively, $\Omega_{\mathbf{q}}$ is the phonon frequency, and α_F is the Fröhlich interaction constant related to the macroscopic properties of the material. In the simplest model with one type of optical phonons

$$\alpha_F = - \left(\frac{2\pi\hbar\Omega}{\varepsilon^*\mathcal{V}} \right)^{1/2}, \quad \frac{1}{\varepsilon^*} = \frac{1}{\varepsilon_\infty} - \frac{1}{\varepsilon_s}, \quad (7)$$

where \mathcal{V} is the normalization volume, ε_s and ε_∞ are the static and high-frequency dielectric constants, respectively, and the dependence of Ω on q is neglected. Hence, LO phonons create an electric field

$$\mathcal{E}_{\mathbf{q}} = -\nabla\varphi_{\mathbf{q}} = \alpha_F \frac{\mathbf{q}}{q} \left(\hat{b}_{\mathbf{q}} e^{i\mathbf{q}\mathbf{r} - i\Omega_{\mathbf{q}}t} + \hat{b}_{\mathbf{q}}^\dagger e^{-i\mathbf{q}\mathbf{r} + i\Omega_{\mathbf{q}}t} \right). \quad (8)$$

By virtue of spin-orbit interaction, this electric field induces a Rashba-like spin-orbit coupling that results in a spin-phonon interaction described by

$$\mathcal{H}_{sf} = \alpha_R \left\{ [\hat{\mathbf{k}} \times \mathcal{E}] \right\}_{\text{sym}} \cdot \hat{\boldsymbol{\sigma}}, \quad (9)$$

where α_R is the Rashba constant related to the spin-orbit interaction, $\hat{\mathbf{k}} = -i\nabla$ is the electron wavevector operator, and $\hat{\boldsymbol{\sigma}}$ is the pseudovector composed of the spin-Pauli matrices representing the electron spin $\hat{\mathbf{s}} = \hat{\boldsymbol{\sigma}}/2$. The curly brackets in Eq. (9) stand for the symmetrization of the operators $\{AB\}_{\text{sym}} = (AB + BA)/2$ since, generally, $\hat{\mathbf{k}}$ does not commute with the coordinate-dependent electric field. Equation (9) represents the so-called direct spin-phonon coupling [40, 46, 47].

The two-phonon contribution to the spin-flip rate at low temperatures $k_B T \ll \hbar\Omega_{\mathbf{q}}$ is related to a process, where one phonon is absorbed and another one is emitted (Raman-like process). These processes are accompanied by virtual transitions of electrons from the ground (g) to the excited (e) state of the NC and back. A sketch of these processes is shown in the inset of Fig. 3(c), where two contributions to the spin-flip matrix element are seen:

$$M_{\downarrow\uparrow} = M^{(1)} + M^{(2)}. \quad (10)$$

The process where the upwards transition is accompanied by an electron spin flip, while the subsequent downwards transition is spin-conserving is described by the term $M^{(1)}$; the opposite case is described by the term $M^{(2)}$. We note that optical phonons in NCs are confined

due to the mismatch between the dielectric properties of the crystal and the matrix. The details and specific models can be found, e.g., in Refs. [48–50]. The electron-phonon interaction is described in Refs. [50, 51]. However, for estimates, we use the long-wavelength approximation assuming that $q \ll 1/a$, where a is the typical NC size. Although this approximation may not be fulfilled in experiment, it allows us to obtain a compact and reasonable analytical estimate. As a result, we can neglect the coordinate dependence of the field \mathcal{E} in Eqs. (8) and (9) and use the spin-independent interaction in the form

$$\mathcal{H}_{orb} = -e\mathcal{E} \cdot \mathbf{r}. \quad (11)$$

Let us now calculate the total matrix element (10) assuming that initially we have an electron in the state $g \uparrow$ and a phonon with wavevector \mathbf{q}_1 , while in the final state we have an electron in the state $g \downarrow$ and a phonon with wavevector \mathbf{q}_2 . Hence, the phonon \mathbf{q}_1 is absorbed and the phonon \mathbf{q}_2 is emitted. We then have

$$M^{(1)}(\mathbf{q}_1, \mathbf{q}_2) = -M^{(2)}(\mathbf{q}_2, \mathbf{q}_1) = \frac{M_{ge}^{(em)}(\mathbf{q}_2)M_{eg}^{(abs,sf)}(\mathbf{q}_1)}{\Delta_{eg} - \hbar\Omega_1} - \frac{M_{ge}^{(abs)}(\mathbf{q}_1)M_{eg}^{(em,sf)}(\mathbf{q}_2)}{\Delta_{eg} + \hbar\Omega_2}. \quad (12)$$

Here, $M_{ge}^{(em)}$ and $M_{eg}^{(em,sf)}$ are the matrix elements of the Hamiltonian terms (11) and (9) describing transitions between NC states without and with spin flip, respectively, involving emission of an optical phonon; correspondingly $M_{ge}^{(abs)}$ and $M_{eg}^{(abs,sf)}$ describe transitions involving absorption of an optical phonon. The specific expressions for the matrix elements are given in the Appendix. Equation (12) is written as if there is only one excited state in a quantum dot. In general, the sum over all states e should be carried out in the matrix element.

The relaxation rate reads

$$\Gamma_{\downarrow\uparrow} = \frac{2\pi}{\hbar} \sum_{\mathbf{q}_1, \mathbf{q}_2} |M_{\downarrow\uparrow}|^2 \Delta_\gamma(\hbar\Omega_1 - \hbar\Omega_2 - g\mu_B B). \quad (13)$$

Here, for definiteness, Ω_1 and Ω_2 are the frequencies of the first and second phonon, the choice of signs corresponds to which of the phonons is emitted or absorbed, and

$$\Delta_\gamma(x) = \frac{1}{\pi} \frac{\hbar\gamma}{x^2 + (\hbar\gamma)^2} \quad (14)$$

is the broadened δ -function that accounts for the finite phonon lifetime $1/\gamma$ [45, 52]. We assume that this broadening is large in comparison to the electron Zeeman splitting ($\hbar\gamma \gg |g\mu_B B|$) and to the relevant range of the optical-phonon dispersion. The latter is restricted by the condition $qa \ll 1$, otherwise the corresponding matrix elements are beyond the long-wavelength approximation and are suppressed. Furthermore, we assume that $\hbar\Omega_1 \approx \hbar\Omega_2 = \hbar\Omega_{LO} \ll \Delta_{eg}$. We also assume that the

temperature is large enough, so that $k_B T \gg |g\mu_B B|$, but $\hbar\Omega \ll k_B T$.

After some algebra, presented in the Appendix and restricting the summation over \mathbf{q}_1 and \mathbf{q}_2 in Eq. (13) to the range of wavevectors satisfying the long-wavelength condition, we arrive at the following expression for the transition rate:

$$\Gamma_{\downarrow\uparrow} = \frac{4C_\chi^2}{27\pi^2} \left(\frac{\varepsilon_s}{\varepsilon^*}\right)^2 \left(\frac{a}{a_B}\right)^2 \frac{(\hbar\Omega_{\text{LO}})^4}{\hbar^2\gamma} \left(\frac{m\alpha_R}{e\hbar^2}\right)^2 \times \exp\left(-\frac{\hbar\Omega_{\text{LO}}}{k_B T}\right), \quad (15)$$

where $a_B = \hbar^2\varepsilon_s/(me^2)$ is the effective Bohr radius, m is the electron effective mass, and C_χ is a numerical factor depending on the shape of the NC.

The Rashba constant α_R in perovskites can be evaluated following the approach for bulk semiconductors presented in Ref. [53] (see also [54]):

$$\left|\frac{\alpha_R}{e}\right| = \frac{P^2}{3E_g^2}, \quad (16)$$

where E_g is the band gap in the perovskite (determined as the energy distance between the Γ_7^- conduction and the Γ_6^+ valence band), $P = (\hbar/m_0)p$, m_0 is the free electron mass, and $p \equiv p_{\parallel} = p_{\perp}$ is the interband momentum matrix element (we assume the cubic phase for simplicity), see Refs. [17, 37]. The description of the band structure and the corresponding parameters are presented in Ref. [17].

We see that Eq. (15) resembles the temperature-dependent part of Eq. (5) used for fitting the experimental dependence with $E_a = \hbar\Omega_{\text{LO}}$. We note that this equation does not contain any dependence on the magnetic field. In our case the Zeeman splitting is much smaller than the phonon linewidth, and the energy conservation is basically fulfilled regardless the details of the phonon spectra. In high fields, when the condition $\hbar\gamma \gg |g\mu_B B|$ is not fulfilled, the situation is more complex, and single acoustic phonons may become important.

Let us use Eq. (15) to estimate the prefactor γ_a in Eq. (5). For estimation purposes, we take $C_\chi = 1$, $\varepsilon_s = 30$, $\varepsilon^* = 6$, $a/a_B \sim 1$, $P \approx 5 \text{ eV\AA}$, $E_g \approx 1.7 \text{ eV}$,

$m = 0.18m_0$ [17], $\hbar\Omega_{\text{LO}} = 3.2 \text{ meV}$, and $\gamma = 0.2 \text{ ps}^{-1}$; the last two values are based on the experimental data of Ref. [42, 45]. With these values, we get an estimate for the exponent prefactor of $\gamma_a = 2 \mu\text{s}^{-1}$. Despite the approximations used and the rather arbitrary parameter choice, this estimate fits the experimental value within an order of magnitude. More importantly, the model reproduces the activation-like character of the T_1 temperature dependence, revealing the relevance of the two-LO-phonon mechanism of spin relaxation in perovskite NCs.

VI. CONCLUSIONS

We have measured ODMR resonances for electrons and holes in CsPbI₃ NCs and determined the key spin parameters: the g factors and their spread, the longitudinal spin relaxation times T_1 , and the effective nuclear fields resulting from the hyperfine interaction. The electron spin relaxation time T_1 is found to be twice longer than the T_1 for holes. We show that the electron T_1 strongly increases when the magnetic field is varied from 0 to 50 mT and saturates at higher fields. This behavior can be explained by the suppression of the impact of the time-varying effective Overhauser nuclear fields; from our data, we can determine the characteristic time of their variation $\tau_c \approx 60 \mu\text{s}$. At low laser powers and in strong magnetic fields, an electron spin relaxation time as long as 0.9 ms is found. We observe an activation-like enhancement of the spin relaxation with increasing temperature and describe it using a model based on a two-LO-phonon Raman process. This study suggests perovskite NCs in a glass matrix as a promising artificially created confined system for spintronics applications.

VII. ACKNOWLEDGMENTS

We acknowledge fruitful discussions with M. O. Nestoklon. V.V.B. and D.R.Y. acknowledge support of the Deutsche Forschungsgemeinschaft (Project YA 65/28-1, No. 527080192). E.V.K. and M.S.K. acknowledge support by the Saint Petersburg State University (Grant No. 125022803069-4).

VIII. APPENDIX

We consider a NC with the symmetry of a cuboid (rectangular parallelepiped) with x , y , and z being its principal axes. The ground state is described by a fully symmetric function $g(\mathbf{r})$. To begin with, let us consider only one intermediate excited state e described by a function $e(\mathbf{r})$ that transforms as the y coordinate, as shown in Fig. 3(c). For example, in a NC with infinitely high potential barriers, these functions are

$$g(\mathbf{r}) = \mathcal{N}_g \cos\left(\frac{\pi x}{a_x}\right) \cos\left(\frac{\pi y}{a_y}\right) \cos\left(\frac{\pi z}{a_z}\right), \quad e(\mathbf{r}) = \mathcal{N}_e \cos\left(\frac{\pi x}{a_x}\right) \sin\left(\frac{2\pi y}{a_y}\right) \cos\left(\frac{\pi z}{a_z}\right),$$

where a_x, a_y, a_z are the lengths of the cuboid's edges and $\mathcal{N}_g, \mathcal{N}_e$ are the normalization constants. A similar analysis for all other intermediate excited states is presented below.

The relevant matrix elements introduced in Eq. (12) take the form:

$$M_{eg}^{(abs)}(\mathbf{q}) = -e\alpha_F\sqrt{n_q}\frac{q_y}{q}\langle e|y|g\rangle, \quad (17a)$$

$$M_{eg}^{(em)}(\mathbf{q}) = -e\alpha_F\sqrt{n_q+1}\frac{q_y}{q}\langle e|y|g\rangle, \quad (17b)$$

$$M_{ge}^{(abs)}(\mathbf{q}) = -e\alpha_F\sqrt{n_q}\frac{q_y}{q}\langle g|y|e\rangle = M_{eg}^{(abs)}(\mathbf{q}), \quad (17c)$$

$$M_{ge}^{(em)}(\mathbf{q}) = -e\alpha_F\sqrt{n_q+1}\frac{q_y}{q}\langle g|y|e\rangle = M_{eg}^{(em)}(\mathbf{q}), \quad (17d)$$

for the spin-conserving processes, and

$$M_{eg}^{(abs,sf)}(\mathbf{q}) = \alpha_F\alpha_R\sqrt{n_q}\frac{q_z}{q}\langle e|\hat{k}_y|g\rangle, \quad (17e)$$

$$M_{eg}^{(em,sf)}(\mathbf{q}) = \alpha_F\alpha_R\sqrt{n_q+1}\frac{q_z}{q}\langle e|\hat{k}_y|g\rangle, \quad (17f)$$

$$M_{ge}^{(abs,sf)}(\mathbf{q}) = \alpha_F\alpha_R\sqrt{n_q}\frac{q_z}{q}\langle g|\hat{k}_y|e\rangle = -M_{eg}^{(abs,sf)}(\mathbf{q}), \quad (17g)$$

$$M_{ge}^{(em,sf)}(\mathbf{q}) = \alpha_F\alpha_R\sqrt{n_q+1}\frac{q_z}{q}\langle g|\hat{k}_y|e\rangle = -M_{eg}^{(em,sf)}(\mathbf{q}), \quad (17h)$$

for the spin-flip processes. Here, we made use of the relations

$$\langle e|y|g\rangle = \langle g|y|e\rangle, \quad \langle e|\hat{k}_y|g\rangle = -\langle g|\hat{k}_y|e\rangle,$$

which are valid for the real wavefunctions of the initial and intermediate states. The filling factors $\sqrt{n_q}$ and $\sqrt{n_q+1}$ appear from the matrix elements of the annihilation and creation operators acting between the states with n_q and $n_q \pm 1$ phonons. Strictly speaking, statistical averaging over the phonon distribution should be carried out in the expression for the transition rate. However, in the case where the phonon modes are uncorrelated and the result is linear in the occupancies of each mode, statistical averaging does not change the result.

For the total matrix element we get

$$\begin{aligned} M^{(1)}(\mathbf{q}_1, \mathbf{q}_2) &= -\frac{M_{ge}^{(em)}(\mathbf{q}_2)M_{eg}^{(abs,sf)}(\mathbf{q}_1)}{\Delta_{eg} - \hbar\Omega_1} - \frac{M_{ge}^{(abs)}(\mathbf{q}_1)M_{eg}^{(em,sf)}(\mathbf{q}_2)}{\Delta_{eg} + \hbar\Omega_2} \\ &= \frac{e\alpha_R\alpha_F^2}{q_1q_2}\sqrt{n_{q_1}(1+n_{q_2})}\langle e|y|g\rangle\langle e|\hat{k}_y|g\rangle\left(\frac{q_{2,y}q_{1,z}}{\Delta_{eg} - \hbar\Omega_1} + \frac{q_{1,y}q_{2,z}}{\Delta_{eg} + \hbar\Omega_2}\right), \end{aligned} \quad (18a)$$

and

$$\begin{aligned} M^{(2)}(\mathbf{q}_1, \mathbf{q}_2) &= -\frac{M_{ge}^{(em,sf)}(\mathbf{q}_2)M_{eg}^{(abs)}(\mathbf{q}_1)}{\Delta_{eg} - \hbar\Omega_1} - \frac{M_{ge}^{(abs,sf)}(\mathbf{q}_1)M_{eg}^{(em)}(\mathbf{q}_2)}{\Delta_{eg} + \hbar\Omega_2} \\ &= -\frac{e\alpha_R\alpha_F^2}{q_1q_2}\sqrt{n_{q_1}(1+n_{q_2})}\langle e|y|g\rangle\langle e|\hat{k}_y|g\rangle\left(\frac{q_{2,z}q_{1,y}}{\Delta_{eg} - \hbar\Omega_1} + \frac{q_{1,z}q_{2,y}}{\Delta_{eg} + \hbar\Omega_2}\right), \end{aligned} \quad (18b)$$

Note that $M^{(1)}(\mathbf{q}_1, \mathbf{q}_2) = -M^{(2)}(\mathbf{q}_2, \mathbf{q}_1)$.

Taking into account that $\hbar\Omega_1 \approx \hbar\Omega_2 = \hbar\Omega_{LO} \ll \Delta_{eg}$ we expand the fractional expressions in Eqs. (18) in a series in $\hbar\Omega_{LO}/\Delta_{eg}$ neglecting the difference between Ω_1 and Ω_2 . As a result, we have

$$M_{\downarrow\uparrow} = M^{(1)}(\mathbf{q}_1, \mathbf{q}_2) + M^{(2)}(\mathbf{q}_1, \mathbf{q}_2) = \frac{2e\alpha_R\alpha_F^2\hbar\Omega_{LO}}{q_1q_2\Delta_{eg}^2}\sqrt{n_{q_1}(1+n_{q_2})}\langle e|y|g\rangle\langle e|\hat{k}_y|g\rangle[\mathbf{q}_2 \times \mathbf{q}_1]_x. \quad (19)$$

Since

$$\langle e|\hat{k}_y|g\rangle = \frac{m}{\hbar}\langle e|dy/dt|g\rangle = \frac{m}{\hbar}\langle e|\frac{i}{\hbar}[\mathcal{H}, y]|g\rangle = \frac{im}{\hbar^2}\Delta_{eg}\langle e|y|g\rangle, \quad (20)$$

where \mathcal{H} is the Hamiltonian describing the quantum-confinement effect, we obtain

$$M_{\downarrow\uparrow} = \frac{im}{\hbar^2} \frac{2e\alpha_R\alpha_F^2\hbar\Omega_{\text{LO}}}{q_1q_2\Delta_{eg}} \sqrt{n_{q_1}(1+n_{q_2})} |\langle e|y|g\rangle|^2 [\mathbf{q}_2 \times \mathbf{q}_1]_x. \quad (21)$$

Introducing the static electronic polarizability tensor of the NC with the principal matrix elements ($i = x, y, z$ [55])

$$\chi_{ii} = \sum_e \frac{2e^2 |\langle e|r_i|g\rangle|^2}{\Delta_{eg}}, \quad r_x = x, \quad r_y = y, \quad r_z = z, \quad (22)$$

where the summation involves all excited states e , and taking into account the similar set of excited states that transform like the x coordinate, we arrive at the following expression for the spin-dependent part of the matrix element

$$\hat{M} = \frac{im}{\hbar^2} (\alpha_R/e) \alpha_F^2 \sqrt{n_{q_1}(1+n_{q_2})} \hbar\Omega_{\text{LO}} \frac{\chi_{yy}[\mathbf{q}_2 \times \mathbf{q}_1]_x \hat{\sigma}_x + \chi_{xx}[\mathbf{q}_2 \times \mathbf{q}_1]_y \hat{\sigma}_y}{q_2q_1}. \quad (23)$$

Thus, the transition rate [Eq. (13)] reads

$$\Gamma_{\downarrow\uparrow} = \exp\left(-\frac{\hbar\Omega_{\text{LO}}}{k_B T}\right) \sum_{\mathbf{q}_1\mathbf{q}_2} \frac{2\pi}{\hbar} \left| \frac{m}{\hbar^2} (\alpha_R/e) \alpha_F^2 \hbar\Omega_{\text{LO}} \right|^2 (\chi_{xx}^2 + \chi_{yy}^2) \times \frac{1}{\pi\hbar\gamma} \times \frac{2}{3}. \quad (24)$$

Here, the factor $2/3$ comes from angular averaging. The sum over $\mathbf{q}_{1,2}$ should be restricted to the range of wavevectors where the long-wavelength approximation holds,

$$\sum_{\mathbf{q}_1\mathbf{q}_2} \dots \sim \left(\frac{\mathcal{V}}{(2\pi)^3}\right)^2 (4\pi)^2 \int_0^{a^{-1}} q_1^2 dq_1 \int_0^{a^{-1}} q_2^2 dq_2 = \frac{\mathcal{V}^2}{36\pi^4 a^6}.$$

Combining all factors, we obtain

$$\Gamma_{\downarrow\uparrow} = \frac{4}{27\pi^2} \exp\left(-\frac{\hbar\Omega_{\text{LO}}}{k_B T}\right) \frac{1}{\hbar^2\gamma} \left(\frac{m\alpha_R}{e\hbar^2}\right)^2 \frac{(\hbar\Omega_{\text{LO}})^3}{(\varepsilon^*)^2} \frac{\chi_{xx}^2 + \chi_{yy}^2}{a^6}. \quad (25)$$

The susceptibility $\sqrt{\chi_{xx}^2 + \chi_{yy}^2} = C_\chi \varepsilon_0 a^4 / a_B$, where $a_B = \hbar^2 \varepsilon_0 / (me^2)$ and C_χ is the numerical factor depending on the shape of the wavefunctions. Hence, Eq. (25) can be rewritten in the form convenient for numerical estimates

$$\Gamma_{\downarrow\uparrow} = \frac{4C_\chi^2}{27\pi^2} \left(\frac{\varepsilon_0}{\varepsilon^*}\right)^2 \left(\frac{a}{a_B}\right)^2 \exp\left(-\frac{\hbar\Omega_{\text{LO}}}{k_B T}\right) \frac{(\hbar\Omega_{\text{LO}})^4}{\hbar^2\gamma} \left(\frac{m\alpha_R}{e\hbar^2}\right)^2. \quad (26)$$

-
- [1] M. Liu, M. B. Johnston, and H. J. Snaith, Efficient planar heterojunction perovskite solar cells by vapour deposition, *Nature* **501**, 395 (2013).
- [2] M. A. Green, A. Ho-Baillie, and H. J. Snaith, The emergence of perovskite solar cells, *Nature Photonics* **8**, 506 (2014).
- [3] J. Han, K. Park, S. Tan, Y. Vaynzof, J. Xue, E. W.-G. Diau, M. G. Bawendi, J.-W. Lee, and I. Jeon, Perovskite solar cells, *Nature Reviews Methods Primers* **5**, 3 (2025).
- [4] C. C. Stoumpos, C. D. Malliakas, J. A. Peters, Z. Liu, M. Sebastian, J. Im, T. C. Chasapis, A. C. Wibowo, D. Y. Chung, A. J. Freeman, B. W. Wessels, and M. G. Kanatzidis, Crystal growth of the perovskite semiconductor CsPbBr₃: a new material for high-energy radiation detection, *Crystal Growth and Design* **13**, 2722 (2013).
- [5] S. Yakunin, M. Sytnyk, D. Kriegner, S. Shrestha, M. Richter, G. J. Matt, H. Azimi, C. J. Brabec, J. Stangl, M. V. Kovalenko, and W. Heiss, Detection of X-ray photons by solution-processed lead halide perovskites, *Nature Photonics* **9**, 444 (2015).
- [6] Y. Cao, N. Wang, H. Tian, J. Guo, Y. Wei, H. Chen, Y. Miao, W. Zou, K. Pan, Y. He, H. Cao, Y. Ke, M. Xu, Y. Wang, M. Yang, K. Du, Z. Fu, D. Kong, D. Dai, Y. Jin, G. Li, H. Li, Q. Peng, J. Wang, and W. Huang, Perovskite light-emitting diodes based on spontaneously formed submicrometre-scale structures, *Nature* **562**, 249 (2018).
- [7] X.-K. Liu, W. Xu, S. Bai, Y. Jin, J. Wang, R. H. Friend,

- and F. Gao, Metal halide perovskites for light-emitting diodes, *Nature Materials* **20**, 10 (2021).
- [8] M. V. Kovalenko, L. Protesescu, and M. I. Bodnarchuk, Properties and potential optoelectronic applications of lead halide perovskite nanocrystals, *Science* **358**, 745 (2017).
- [9] H. Utzat, W. Sun, A. E. K. Kaplan, F. Krieg, M. Ginterseder, B. Spokoyny, N. D. Klein, K. E. Shulenberger, C. F. Perkinson, M. V. Kovalenko, and M. G. Bawendi, Coherent single-photon emission from colloidal lead halide perovskite quantum dots, *Science* **363**, 1068 (2019).
- [10] L. Protesescu, S. Yakunin, M. I. Bodnarchuk, F. Krieg, R. Caputo, C. H. Hendon, R. X. Yang, A. Walsh, and M. V. Kovalenko, Nanocrystals of Cesium lead halide perovskites (CsPbX_3 , X = Cl, Br, and I): novel optoelectronic materials showing bright emission with wide color gamut, *Nano Letters* **15**, 3692 (2015).
- [11] E. V. Kolobkova, M. S. Kuznetsova, and N. V. Nikonorov, Perovskite CsPbX_3 (X=Cl, Br, I) nanocrystals in fluorophosphate glasses, *Journal of Non-Crystalline Solids* **563**, 120811 (2021).
- [12] M. O. Nestoklon, S. V. Goupalov, R. I. Dzhioev, O. S. Ken, V. L. Korenev, Y. G. Kusrayev, V. F. Sapega, C. de Weerd, L. Gomez, T. Gregorkiewicz, J. Lin, K. Suenaga, Y. Fujiwara, L. B. Matyushkin, and I. N. Yassievich, Optical orientation and alignment of excitons in ensembles of inorganic perovskite nanocrystals, *Physical Review B* **97**, 235304 (2018).
- [13] P. Odenthal, W. Talmadge, N. Gundlach, R. Wang, C. Zhang, D. Sun, Z.-G. Yu, Z. Valy Vardeny, and Y. S. Li, Spin-polarized exciton quantum beating in hybrid organic-inorganic perovskites, *Nature Physics* **13**, 894 (2017).
- [14] V. V. Belykh, D. R. Yakovlev, M. M. Glazov, P. S. Grigoryev, M. Hussain, J. Rautert, D. N. Dirin, M. V. Kovalenko, and M. Bayer, Coherent spin dynamics of electrons and holes in CsPbBr_3 perovskite crystals, *Nature Communications* **10**, 673 (2019).
- [15] M. J. Crane, L. M. Jacoby, T. A. Cohen, Y. Huang, C. K. Luscombe, and D. R. Gamelin, Coherent Spin Precession and Lifetime-Limited Spin Dephasing in CsPbBr_3 Perovskite Nanocrystals, *Nano Letters* **20**, 8626 (2020).
- [16] P. S. Grigoryev, V. V. Belykh, D. R. Yakovlev, E. Lhuillier, and M. Bayer, Coherent spin dynamics of electrons and holes in CsPbBr_3 colloidal nanocrystals, *Nano Letters* **21**, 8481 (2021).
- [17] E. Kirstein, D. R. Yakovlev, M. M. Glazov, E. A. Zhukov, D. Kudlacik, I. V. Kalitukha, V. F. Sapega, G. S. Dimitriev, M. A. Semina, M. O. Nestoklon, E. L. Ivchenko, N. E. Kopteva, D. N. Dirin, O. Nazarenko, M. V. Kovalenko, A. Baumann, J. Höcker, V. Dyakonov, and M. Bayer, The Landé factors of electrons and holes in lead halide perovskites: universal dependence on the band gap, *Nature Communications* **13**, 3062 (2022).
- [18] M. O. Nestoklon, E. Kirstein, D. R. Yakovlev, E. A. Zhukov, M. M. Glazov, M. A. Semina, E. L. Ivchenko, E. V. Kolobkova, M. S. Kuznetsova, and M. Bayer, Tailoring the electron and hole Landé factors in lead halide perovskite nanocrystals by quantum confinement and halide exchange, *Nano Letters* **23**, 8218 (2023).
- [19] E. Kirstein, D. R. Yakovlev, E. A. Zhukov, N. E. Kopteva, B. Turedi, M. V. Kovalenko, and M. Bayer, Resonant spin amplification and accumulation in MAPbI_3 single crystals, *Advanced Science* **12**, 2502735 (2025).
- [20] S. R. Meliakov, E. A. Zhukov, V. V. Belykh, M. O. Nestoklon, E. V. Kolobkova, M. S. Kuznetsova, M. Bayer, and D. R. Yakovlev, Landé g -factors of electrons and holes strongly confined in CsPbI_3 perovskite nanocrystals in glass, *Nanoscale* **17**, 6522 (2025).
- [21] J. Zhu, Y. Li, X. Lin, Y. Han, and K. Wu, Coherent phenomena and dynamics of lead halide perovskite nanocrystals for quantum information technologies, *Nature Materials* **23**, 1027 (2024).
- [22] P. Tamarat, M. I. Bodnarchuk, J.-B. Trebbia, R. Erni, M. V. Kovalenko, J. Even, and B. Lounis, The ground exciton state of formamidinium lead bromide perovskite nanocrystals is a singlet dark state, *Nature Materials* **18**, 717 (2019).
- [23] Z. G. Yu, Effective-mass model and magneto-optical properties in hybrid perovskites, *Scientific Reports* **6**, 28576 (2016).
- [24] E. Kirstein, D. R. Yakovlev, M. M. Glazov, E. Evers, E. A. Zhukov, V. V. Belykh, N. E. Kopteva, D. Kudlacik, O. Nazarenko, D. N. Dirin, M. V. Kovalenko, and M. Bayer, Lead-dominated hyperfine interaction impacting the carrier spin dynamics in halide perovskites, *Advanced Materials* **34**, 2105263 (2022).
- [25] M. Kotur, P. S. Bazhin, K. V. Kavokin, N. E. Kopteva, D. R. Yakovlev, D. Kudlacik, and M. Bayer, Dynamic polarization of nuclear spins by optically oriented electrons and holes in lead halide perovskite semiconductors, *Physical Review B* **113**, 085204 (2026).
- [26] X. Lin, Y. Han, J. Zhu, and K. Wu, Room-temperature coherent optical manipulation of hole spins in solution-grown perovskite quantum dots, *Nature Nanotechnology* **18**, 124 (2023).
- [27] S. R. Meliakov, E. A. Zhukov, E. V. Kulebyakina, V. V. Belykh, and D. R. Yakovlev, Coherent Spin Dynamics of Electrons in CsPbBr_3 Perovskite Nanocrystals at Room Temperature, *Nanomaterials* **13**, 2454 (2023).
- [28] N. E. Kopteva, D. R. Yakovlev, E. Yalcin, I. A. Akimov, M. O. Nestoklon, M. M. Glazov, M. Kotur, D. Kudlacik, E. A. Zhukov, E. Kirstein, O. Hordiichuk, D. N. Dirin, M. V. Kovalenko, and M. Bayer, Highly-polarized emission provided by giant optical orientation of exciton spins in lead halide perovskite crystals, *Advanced Science* **11**, 2403691 (2024).
- [29] N. E. Kopteva, D. R. Yakovlev, E. Yalcin, I. V. Kalitukha, I. A. Akimov, M. O. Nestoklon, B. Turedi, O. Hordiichuk, D. N. Dirin, M. V. Kovalenko, and M. Bayer, Effect of crystal symmetry of lead halide perovskites on the optical orientation of excitons, *Advanced Science* **12**, 2416782 (2025).
- [30] D. Kudlacik, N. E. Kopteva, M. Kotur, D. R. Yakovlev, K. V. Kavokin, C. Harkort, M. Karzel, E. A. Zhukov, E. Evers, V. V. Belykh, and M. Bayer, Optical spin orientation of localized electrons and holes interacting with nuclei in a $\text{FA}_{0.9}\text{Cs}_{0.1}\text{PbI}_{2.8}\text{Br}_{0.2}$ perovskite crystal, *ACS Photonics* **11**, 2757 (2024).
- [31] V. V. Belykh and S. R. Melyakov, Selective measurement of the longitudinal electron spin relaxation time T_1 of Ce^{3+} ions in a YAG lattice: Resonant spin inertia, *Physical Review B* **105**, 205129 (2022).
- [32] V. V. Belykh, M. L. Skorikov, E. V. Kulebyakina, E. V. Kolobkova, M. S. Kuznetsova, M. M. Glazov, and D. R. Yakovlev, Submillisecond spin relaxation in $\text{CsPb}(\text{Cl},\text{Br})_3$ perovskite nanocrystals in a glass matrix,

- Nano Letters* **22**, 4583 (2022).
- [33] A. Bechtold, D. Rauch, F. Li, T. Simmet, P.-L. Ardel, A. Regler, K. Müller, N. Sinitsyn, and J. J. Finley, Three-stage decoherence dynamics of an electron spin qubit in an optically active quantum dot, *Nature Physics* **11**, 1005 (2015).
- [34] E. Kirstein, N. E. Kopteva, D. R. Yakovlev, E. A. Zhukov, E. V. Kolobkova, M. S. Kuznetsova, V. V. Belykh, I. A. Yugova, M. M. Glazov, M. Bayer, and A. Greilich, Mode locking of hole spin coherences in CsPb(Cl,Br)₃ perovskite nanocrystals, *Nature Communications* **14**, 699 (2023).
- [35] S. R. Meliakov, E. A. Zhukov, V. V. Belykh, M. O. Nestoklon, E. V. Kolobkova, M. S. Kuznetsova, M. Bayer, and D. R. Yakovlev, Temperature dependence of the electron and hole Landé g -factors in CsPbI₃ nanocrystals embedded in a glass matrix, *Nanoscale* **16**, 21496 (2024).
- [36] F. Heisterkamp, E. A. Zhukov, A. Greilich, D. R. Yakovlev, V. L. Korenev, A. Pawlis, and M. Bayer, Longitudinal and transverse spin dynamics of donor-bound electrons in fluorine-doped ZnSe: Spin inertia versus Hanle effect, *Physical Review B* **91**, 235432 (2015).
- [37] M. O. Nestoklon, E. Kirstein, D. R. Yakovlev, E. A. Zhukov, M. M. Glazov, M. A. Semina, E. L. Ivchenko, E. V. Kolobkova, M. S. Kuznetsova, and M. Bayer, Tailoring the electron and hole Landé factors in lead halide perovskite nanocrystals by quantum confinement and halide exchange, *Nano Letters* **23**, 8218 (2023).
- [38] V. V. Belykh, D. R. Yakovlev, J. J. Schindler, E. A. Zhukov, M. A. Semina, M. Yacob, J. P. Reithmaier, M. Benyoucef, and M. Bayer, Large anisotropy of electron and hole g factors in infrared-emitting InAs/InAlGaAs self-assembled quantum dots, *Physical Review B* **93**, 125302 (2016).
- [39] I. Merkulov, A. L. Efros, and M. Rosen, Electron spin relaxation by nuclei in semiconductor quantum dots, *Physical Review B* **65**, 205309 (2002).
- [40] M. M. Glazov, *Electron & Nuclear Spin Dynamics in Semiconductor Nanostructures*, Series on Semiconductor Science and Technology (OUP Oxford, 2018).
- [41] S. R. Meliakov, E. A. Zhukov, V. V. Belykh, K. V. Kavokin, M. O. Nestoklon, E. V. Kulebyakina, M. L. Skorikov, E. V. Kolobkova, M. S. Kuznetsova, M. Bayer, and D. R. Yakovlev, Hyperfine interaction of electrons confined in CsPbI₃ nanocrystals with nuclear spin fluctuations, *Physical Review B* **113**, 035304 (2026).
- [42] C. Harkort, I. V. Kalitukha, N. E. Kopteva, M. O. Nestoklon, S. V. Goupalov, L. Saviot, D. Kudlacik, D. R. Yakovlev, E. V. Kolobkova, M. S. Kuznetsova, and M. Bayer, Confined acoustic phonons in CsPbI₃ nanocrystals explored by resonant Raman scattering on excitons, *Nano Letters* **25**, 12754 (2025).
- [43] E. V. Kulebyakina, M. L. Skorikov, E. V. Kolobkova, M. S. Kuznetsova, M. N. Bataev, D. R. Yakovlev, and V. V. Belykh, Temperature-dependent photoluminescence dynamics of CsPbBr₃ and CsPb(Cl,Br)₃ perovskite nanocrystals in a glass matrix, *Physical Review B* **109**, 235301 (2024).
- [44] D. S. Smirnov, E. A. Zhukov, E. Kirstein, D. R. Yakovlev, D. Reuter, A. D. Wieck, M. Bayer, A. Greilich, and M. M. Glazov, Theory of spin inertia in singly charged quantum dots, *Physical Review B* **98**, 125306 (2018).
- [45] A. V. Trifonov, M. O. Nestoklon, M. A. Hollberg, S. Grisard, D. Kudlacik, E. V. Kolobkova, M. S. Kuznetsova, S. V. Goupalov, J. M. Kaspari, D. E. Reiter, D. R. Yakovlev, M. Bayer, and I. A. Akimov, Quantum beats of exciton-polarons in CsPbI₃ perovskite nanocrystals, arXiv:2510.14695 [10.48550/arXiv.2510.14695](https://arxiv.org/abs/10.48550/arXiv.2510.14695) (2025).
- [46] S. T. Pavlov and Y. A. Firsov, Spin flip interaction of electrons with optical phonons in semiconductors, *Sov. Phys. Solid State* **7**, 2131 (1966).
- [47] S. T. Pavlov and Y. A. Firsov, On spin-phonon interaction of electrons and oscillations of longitudinal magnetoresistance in semiconductors, *Sov. Phys. Solid State* **9**, 1394 (1967).
- [48] R. Englman and R. Ruppin, Optical lattice vibrations in finite ionic crystals: I, *Journal of Physics C: Solid State Physics* **1**, 614 (1968).
- [49] R. Ruppin and R. Englman, Optical phonons of small crystals, *Reports on Progress in Physics* **33**, 149 (1970).
- [50] Al. L. Efros, Electron-hole pair — phonon interaction in semiconductor microcrystals, in *Phonons in Semiconductor Nanostructures*, edited by J.-P. Leburton, J. Pascual, and C. S. Torres (Springer Netherlands, Dordrecht, 1993) pp. 299–308.
- [51] M. C. Klein, F. Hache, D. Ricard, and C. Flytzanis, Size dependence of electron-phonon coupling in semiconductor nanospheres: the case of CdSe, *Phys. Rev. B* **42**, 11123 (1990).
- [52] A. A. Prokofiev, A. N. Poddubny, and I. N. Yassievich, Phonon decay in silicon nanocrystals: Fast phonon recycling, *Physical Review B* **89**, 125409 (2014).
- [53] R. Winkler, *Spin-Orbit Coupling Effects in Two-Dimensional Electron and Hole Systems* (Springer, 2003).
- [54] E. A. Andrada e Silva, G. C. L. Rocca, and F. Bassani, Spin-split subbands and magneto-oscillations in III-V asymmetric heterostructures, *Phys. Rev. B* **50**, 8523 (1994).
- [55] L. D. Landau and E. M. Lifshitz, *Quantum Mechanics: Non-Relativistic Theory* (Butterworth-Heinemann, Oxford, 1977).